The first in situ observation of Kelvin-Helmholtz waves at high-latitude magnetopause during strongly dawnward interplanetary magnetic field conditions

K.-J. Hwang,[1,2] M. L. Goldstein,[1] M. M. Kuznetsova,[3] Y. Wang,[2,3] A. F. Viñas,[1] and D. G. Sibeck[3]

Received 14 October 2011; revised 5 July 2012; accepted 8 July 2012; published 29 August 2012.

[1] We report the first in situ observation of high-latitude magnetopause (near the northern duskward cusp) Kelvin-Helmholtz waves (KHW) by Cluster on January 12, 2003, under strongly dawnward interplanetary magnetic field (IMF) conditions. The fluctuations unstable to Kelvin-Helmholtz instability (KHI) are found to propagate mostly tailward, i.e., along the direction almost 90° to both the magnetosheath and geomagnetic fields, which lowers the threshold of the KHI. The magnetic configuration across the boundary layer near the northern duskward cusp region during dawnward IMF is similar to that in the low-latitude boundary layer under northward IMF, in that (1) both magnetosheath and magnetospheric fields across the local boundary layer constitute the lowest magnetic shear and (2) the tailward propagation of the KHW is perpendicular to both fields. Approximately 3-hour-long periods of the KHW during dawnward IMF are followed by the rapid expansion of the dayside magnetosphere associated with the passage of an IMF discontinuity that characterizes an abrupt change in IMF cone angle, $\phi = \mathrm{acos}\left(\frac{B_x}{|\mathbf{B}|}\right)$, from $\sim$90° to $\sim$10°. Cluster, which was on its outbound trajectory, continued observing the boundary waves at the northern evening-side magnetopause during sunward IMF conditions following the passage of the IMF discontinuity. By comparing the signatures of boundary fluctuations before and after the IMF discontinuity, we report that the frequencies of the most unstable KH modes increased after the discontinuity passed. This result demonstrates that differences in IMF orientations (especially in ϕ) are associated with the properties of KHW at the high-latitude magnetopause due to variations in thickness of the boundary layer, and/or width of the KH-unstable band on the surface of the dayside magnetopause.

Citation: Hwang, K.-J., M. L. Goldstein, M. M. Kuznetsova, Y. Wang, A. F. Viñas, and D. G. Sibeck (2012), The first in situ observation of Kelvin-Helmholtz waves at high-latitude magnetopause during strongly dawnward interplanetary magnetic field conditions, *J. Geophys. Res.*, *117*, A08233, doi:10.1029/2011JA017256.

1. Introduction

[2] Understanding how the interaction of the solar wind with Earth's magnetic field transfers plasma, momentum, and energy across the magnetopause is one of the most important questions in magnetospheric physics. Since *Dungey* [1954] first suggested that the Kelvin-Helmholtz instability (KHI) might play an important role in the dynamics of Earth's low-latitude boundary layer (LLBL) between the fast magnetosheath flow and the relatively stagnant plasma sheet, the Kelvin-Helmholtz (KH) mode has been studied using theoretical analyses, numerical simulations, and in situ observations [e.g., *Southwood*, 1979; *Kivelson and Chen*, 1995; *Miura*, 1995; *Otto and Fairfield*, 2000; *Hasegawa et al.*, 2004].

[3] These studies have been predominantly carried out during periods of northward interplanetary magnetic field (IMF) conditions, which minimizes the magnetic tension forces that stabilize the KHI at the subsolar side of the magnetopause and LLBL. In situ observations of fully developed Kelvin-Helmholtz waves (KHW), i.e., rolled-up KH vortices (KHV), have been reported to occur preferentially for northward IMF [*Hasegawa et al.*, 2009; *Fairfield et al.*, 2000, 2007]. Several explanations for this preference have been suggested, including: competition with a tearing mode that

[1]Code 673, NASA Goddard Space Flight Center, Greenbelt, Maryland, USA.
[2]Code 674, NASA Goddard Space Flight Center, Greenbelt, Maryland, USA.
[3]Goddard Planetary and Heliophysics Institute, University of Maryland, Baltimore County, Baltimore, Maryland, USA.

Corresponding author: K.-J. Hwang, Code 673, NASA Goddard Space Flight Center, Greenbelt, MD 20771, USA. (kyoung-joo.hwang@nasa.gov)

0148-0227/12/2011JA017256

suppresses KHI development for large magnetic shear under southward IMF [*Chen et al.*, 1993, 1997; *Farrugia et al.*, 2003]; the formation of a slow rarefaction region with a magnetic pressure maximum just inside the magnetopause under southward IMF [*Miura*, 1995]; the formation of a thin KH-unstable plasma sheet layer between the northern and southern lobes during southward IMF that stabilizes the KHI due to the intense lobe magnetic field [*Hashimoto and Fujimoto*, 2005]; and, the formation of a dense LLBL resulting from high-latitude reconnection that lowers the threshold of the KHI during northward IMF [*Hasegawa et al.*, 2009].

[4] Interestingly, the KH-unstable condition for incompressible plasmas [*Hasegawa*, 1975], under the assumption that the interface layer has no thickness, shows no preference for northward over southward IMF:

$$[\mathbf{k}\cdot(\mathbf{v}_2-\mathbf{v}_1)]^2 > \frac{1}{\mu_0}\left(\frac{1}{\rho_1}+\frac{1}{\rho_2}\right)\left[(\mathbf{B}_1\cdot\mathbf{k})^2+(\mathbf{B}_2\cdot\mathbf{k})^2\right] \quad (1)$$

where $\mathbf{v}_{1,2}$, $\rho_{1,2}$, and $\mathbf{B}_{1,2}$ represent flow velocity, plasma density, and magnetic field at sides 1 and 2 across the velocity shear interface, respectively, and $\mathbf{k}$ represents the wave vector [*Chandrasekhar*, 1961].

[5] Studies of the competition between the KH and tearing instabilities have found that the tearing instability is dominated by growing KH modes when the Alfvénic Mach number, M_A, associated with the velocity difference across the boundary layer, is large, e.g., when $M_A > 1$ and there is no density gradient across the velocity shear layer [*Fuselier et al.*, 2000]. *La Belle-Hamer et al.* [1995] showed that the threshold M_A for which tearing mode is quenched depends on the density ratio across the boundary layer.

[6] The recent observation of fully developed KHW for southward IMF suggested new insights on the preferential detection of KHW and KHV during northward IMF in the context of an intrinsic discrepancy in the magnetopause behavior under varying IMF conditions [*Hwang et al.*, 2011]: Southward IMF typically generates dynamically active subsolar environments that cause the formation and evolution of KHW to be temporally intermittent and irregular. Such evolution would leave little chance to observe well-developed KHV under southward IMF.

[7] Indeed, magnetohydrodynamics (MHD) simulations [*Kuznetsova et al.*, 2008; *Ogino*, 2009] demonstrated that while the development of KHW/KHV during northward IMF is rather stationary and the structures are long-lasting, under southward IMF, KHV develop quickly, often formed as a filamentary structure that tends to become unstable to subsolar-originated fluctuations such as reconnection and flux ropes that drift along the flank and disrupt any previously formed KHV. These observational and numerical studies suggest the need for further studies of the generation and evolution of KHW under different IMF conditions.

[8] *Kivelson and Chen* [1995] raised a question as to whether or not the quasiperiodicity of the KHW was a consequence of solar wind parameters, e.g., pressure fluctuations, or of intrinsic instabilities of the boundary. They pointed out that the wave power detected by ground magnetometers during the KH activity peaked at different frequencies in the morning and evening sectors, which indicated that the wavelength and frequency of KHW was determined by local plasma conditions. On the other hand, MHD simulations by *Claudepierre et al.* [2008] showed that the frequencies of KHW depend on the solar wind driving velocity—larger driving velocities generate higher-frequency KHW. *Farrugia et al.* [2003], using KHW observations under northward IMF, reported that for the two 2-hour intervals with the average IMF clock angle (the angle of the IMF in the *yz*-plane measured away from the **z**-direction clockwise looking from the Sun to the Earth), $\langle\theta\rangle = 6^\circ$ and 18°, the wavelength of the KHW broadened as the IMF clock angle decreased. They explained this as a consequence of the fact that the KH-unstable bands, depicted by the regions of low magnetic shear ($<10^\circ$) on the surface of the dayside magnetopause, broaden as the IMF clock angle decreases, and hence can support the generation of KHW of longer wavelength [*Farrugia et al.*, 1998].

[9] *Gratton et al.* [2004] analytically solved the KHI condition for the paraboloid dayside magnetopause with a finite thickness across the transition layer. They found that the KHI is unstable for certain magnetic shear angles or solar wind Alfvén Mach number (M_A) for which a thin-boundary model predicts stability against the KHI (although the growth rate of KHI is smaller than low magnetic-shear or high M_A cases). This suggests that the combined effects of solar wind parameters and boundary layer conditions characterize the wave properties of the KH mode.

[10] These previous studies of the effect of IMF parameters on KHW have predominantly addressed the cases of either small variations of IMF clock angle ($<30^\circ$) from northward-pointing IMF, or for strictly northward or southward IMF conditions. Earlier publications [*Greenstadt and Olson*, 1976; *Lee and Olson*, 1980] paid attention to the influence of either (1) the angle between the IMF and the normal of the bow shock on the KHI (for small angles, more wave energy generated at the turbulent sub-solar shock transition region is convected to the magnetopause) or (2) the angle between the magnetosheath field and the magnetospheric field around the magnetopause to explain the local-time variations and dawn-dusk asymmetry in the occurrence rate and the amplitude of the geomagnetic pulsations. (The Parker spiral is tangential to the dusk flank, i.e., to the typical tailward propagation of the KHW, but makes a large angle with the dawn flank, which lowers the KH unstable threshold in the morning-side magnetopause flank.) *Farrugia et al.* [1998] and *Contin et al.* [2003] showed that even for the strongly northward IMF the KHI is tightly regulated by the local magnetic shear angle. Because the magnetosheath field is draped over the magnetopause, the KH growth rate decreases significantly as the latitude increases.

[11] However, previous studies have not developed a detailed understanding about how the generation of KHW and their wave properties are characterized under dawn/dusk-ward or radial (sunward/anti-sunward) IMF orientations. In this paper, we discuss an event that suggests an answer to this question. Such IMF orientations relocate the regions on the surface of the magnetopause where the KHW can easily become unstable. The majority of previously reported in situ observations of KHW/KHV has been detected at the flanks or LLBL of magnetosphere [e.g., *Chen and Kivelson*, 1993; *Fairfield et al.*, 2000; *Farrugia et al.*, 2000; *Hasegawa et al.*, 2004; *Nykyri et al.*, 2006; *Hwang et al.*, 2011]. This event, detected by the Cluster spacecraft, presents the first *in-situ* observation of KHW at the

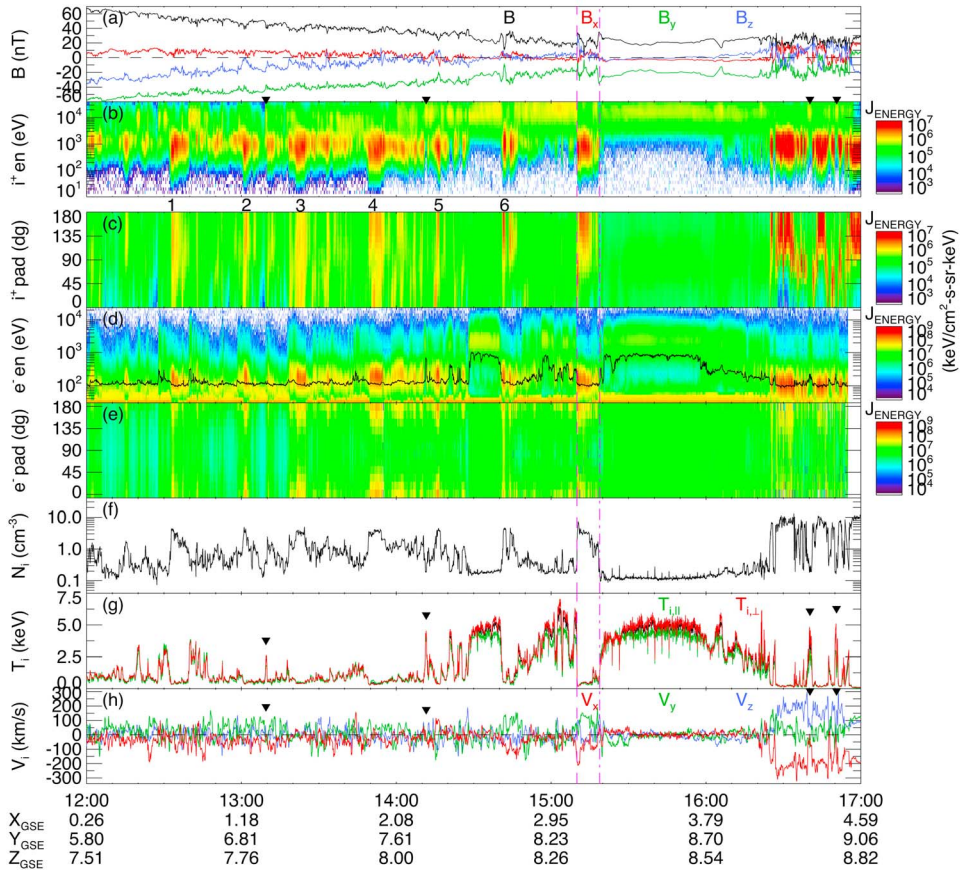

Figure 1. Observations from C1 during 2003-01-12/1200–1700 UT (all the parameters in this and following figures are shown in GSE coordinates.): (a) the magnitude (black) of the magnetic field and the x (red), y (green), and z (blue) component of the magnetic field; (b) the ion energy and (c) pitch angle spectrograms; (d) the electron energy and (e) pitch angle spectrograms; (f) the ion density; (g) the ion parallel, perpendicular, and total temperature measured by C1 (green, red, and black, respectively); (h) the ion velocity, V_x (red), V_y (green), and V_z (blue). A black curve overplotted in Figure 1d represents electron characteristic energy defined by the energy flux divided by the number flux.

high latitude magnetopause, near the northern cusp, during strongly dawnward IMF. About 3-hour-long periods of boundary fluctuations are investigated using the four Cluster spacecraft on its outbound trajectory at the duskside cusp in the northern hemisphere. Following an encounter with the expansion of the dayside magnetosphere associated with the arrival of an IMF discontinuity, Cluster continued observing the boundary waves at the evening side magnetopause. By comparing the signatures of boundary fluctuations before and after the IMF discontinuity, we investigate how differences in IMF orientations (especially, in the IMF cone angle, defined by $\phi = \mathrm{acos}\left(\frac{B_x}{|\mathbf{B}|}\right)$) are associated with the properties of KHW observed at the high-latitude magnetopause.

2. Observations

2.1. Overview of the Event

[12] During 1200–1700 UT on January 12, 2003, the barycenter of the tetrahedron configuration of the four Cluster spacecraft was located near the northern duskward cusp region (around [0.6, 5.3, 7.5] Earth radii (R_E) at 1200 UT), and was outbound toward the evening side northern hemisphere magnetopause (around [4.9, 10.2, 7.0]R_E at 1700 UT), as indicated in Figure 1 by a negative-to-positive change of B_z and a dominant $-B_y$ component. (All parameters throughout this paper are shown in GSE coordinates.)

[13] The magnitude of the magnetic field components ($|\mathbf{B}|$) generally declines until ~1510 UT (Figure 1a), but it also shows repeated short durations of depressed $|\mathbf{B}|$ (especially, $|B_z|$). During those intervals of decreasing $|\mathbf{B}|$, the particle energy spectrograms (Figures 1b and 1d) appear to be more populated by low-energy particles (200–3000 eV for ions, and 70–600 eV for electrons) that are mostly parallel or antiparallel to **B** (Figure 1e). These depressed $|\mathbf{B}|$ periods also correspond to periods of high density (Figure 1f) and low temperature (Figure 1g). That These field and plasma signatures characterize the magnetosheath side of the boundary layer just inside the magentopause (i.e., the outer region of the boundary layer), rather than the magnetosheath region, can be deduced because (1) the magnitude of the magnetic field, which is presumably closed within this boundary, is larger than the solar wind field (Figure 2a), (2) the particle energy spectrograms show still noticeable high-energy populations, and (3) the anti-sunward speed of the bulk plasma flow (V_x in Figure 1h) is far less than the solar wind

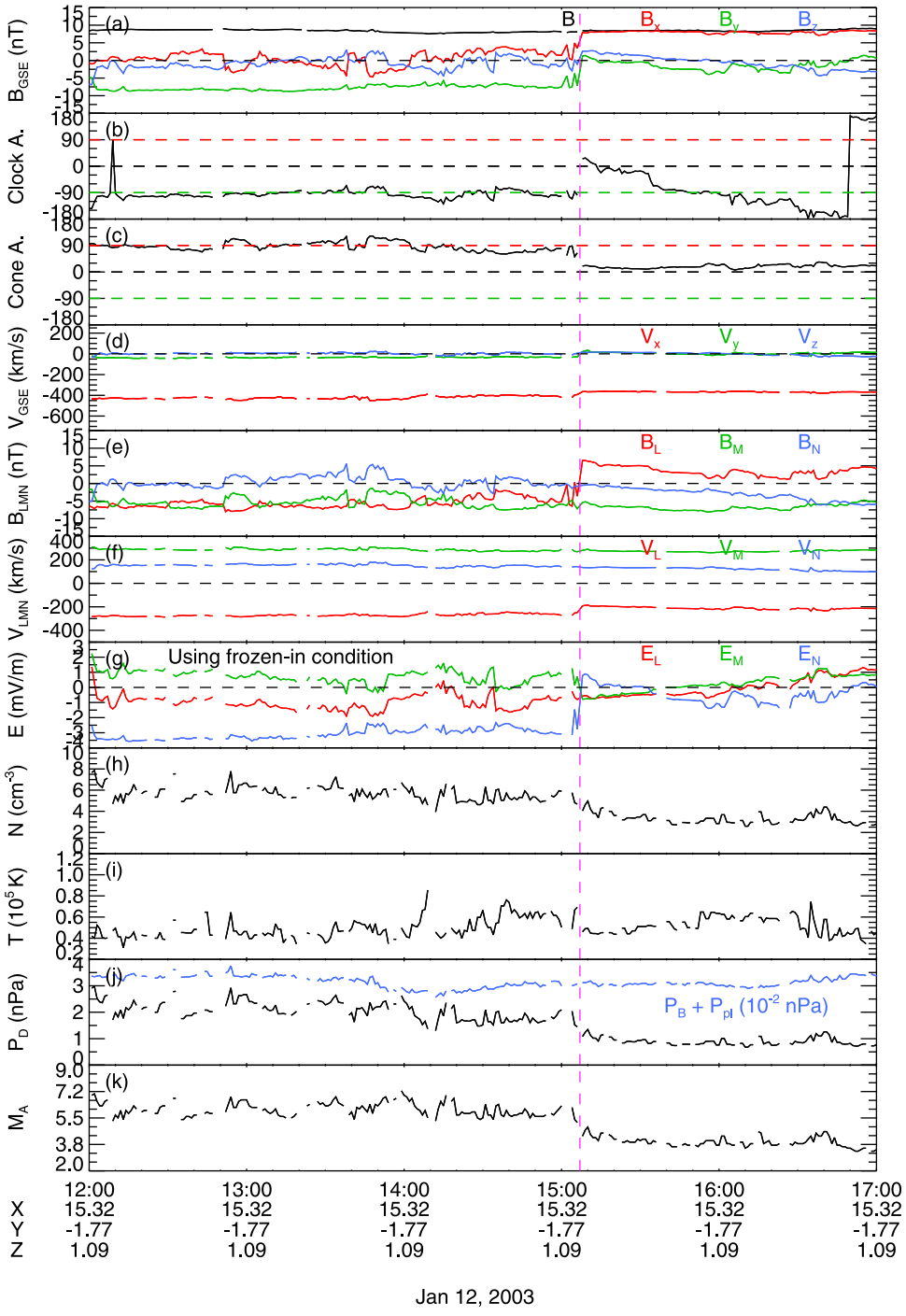

Figure 2. Solar wind conditions from the ACE High Resolution OMNI (HRO) 1-minute-resolution data during the event. IMF and solar wind parameters from ACE are shifted in time according to the travel time of the solar wind to 1 AU at the location of the nose of the model bow shock [*Farris and Russell*, 1994], which are shown at the bottom of this figure.

speed (~400 km/s, Figure 2d). After each encounter with this outer region of the boundary layer, Cluster returns to the region characterized by low density and high temperature (Figures 1f and 1g) that is populated largely with higher-energy particles (Figures 1b and 1d). This region is more-magnetospheric and represents the inner region of the boundary layer. The repeated encounters of Cluster with these two regions of the boundary layer during this interval, 1200–1510 UT, suggests that the boundary layer is fluctuating. Cluster observations of simultaneous variations in plasma components and moments and in magnetic fields are typical signatures of KHW observed in the boundary layer adjacent to the Earth's magnetopause [e.g., *Hasegawa et al.*, 2004].

[14] At ~1510 UT (marked by a magenta dashed vertical line in Figure 1) the particle spectrograms, the density,

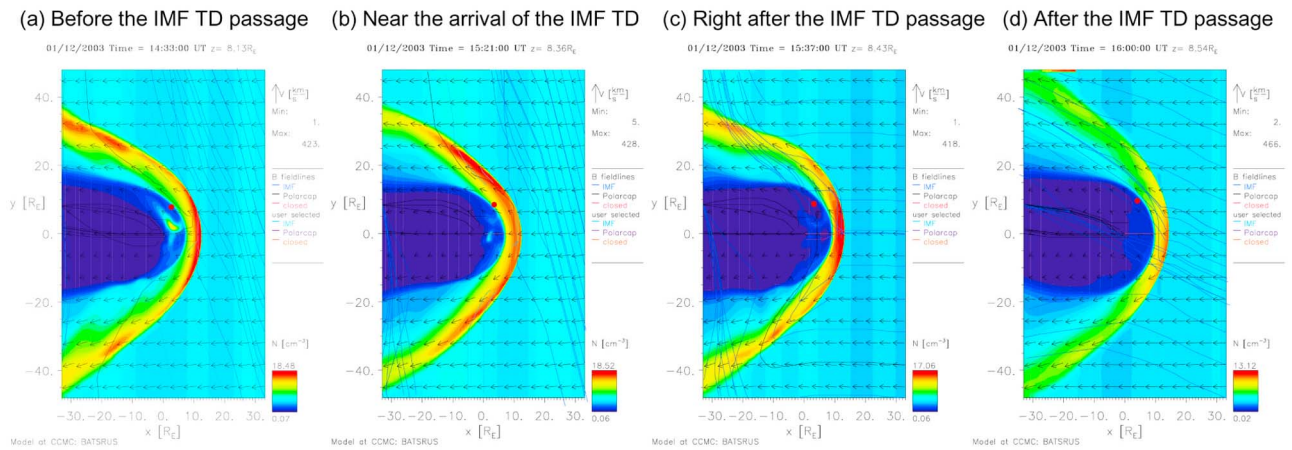

Figure 3. MHD simulation results for the Cluster observations using a BATS-R-US code. Red dots show the locations of Cluster-1 at different times.

temperature, and (anti-sunward) flow velocity show rapid changes that indicate entry into the magnetosheath. After a ~9-minute-long traverse of the more-magnetosheath side of the boundary layer, Cluster entered into the magnetospheric region containing ≥1 keV ions. Cluster remained in the magnetosphere until it re-encountered the boundary layer at 1623–1657 UT. When considering a continuous outbound trajectory of Cluster, the forward-and then-backward motion of Cluster relative to the magnetopause during ~1510–1520 UT can be interpreted as a transient compression of the dayside magnetosphere followed by an expansion.

[15] Figure 2 reveals that this compression and expansion of the dayside magnetosphere, or equivalently the inward and outward motion of the magnetopause, are associated with the IMF discontinuity marked by a magenta dashed vertical line at ~1508 UT. The High Resolution OMNI (HRO) data shown in Figure 2 at 1 minute resolution from ACE, which was located near [238, −25, −22]R_E during the event, provide the time-shifted IMF and solar wind parameters at a model bow shock nose location [*Farris and Russell*, 1994]. Across the discontinuity, the IMF rotates from the mainly negative **y**-direction (IMF clock angle of ~−90°, as shown in Figure 2b) to the positive **x**-direction (Figure 2a): The IMF cone angle ϕ changes from ~90° to ~10° (Figure 2c).

[16] From minimum variance analysis (MVA) of the IMF components, the boundary normal coordinates to the discontinuity are found to be: **l** = [0.58, 0.73, 0.36], **m** = [−0.74, 0.66, −0.14], and **n** = [−0.34, −0.19, 0.92] (the ratio of the medium-to-minimum eigenvalue is 3.46). Figures 2e–2g show the transformed B_{lmn}, V_{lmn}, and E_{lmn} under the assumption of frozen-in flow. There is no velocity jump along the **n** direction (therefore, this is a discontinuity rather than a shock), and the total pressure (the sum of the magnetic pressure and the plasma thermal pressure shown as a blue curve in Figure 2j), does not show a noticeable change. Thus the discontinuity is most likely to be a tangential discontinuity (TD).

[17] Note that the electric field points toward the discontinuity on both sides (E_n = −3 and 1 mV/m before and after the discontinuity, based on the positive **n** component of the solar wind velocity). This signature is important in the formation of Hot Flow Anomalies (HFAs) in the vicinity of the Earth's bow shock as ions reflected from the bow shock are guided back along the TD and expand [*Burgess*, 1989; *Thomas et al.*, 1991; *Eastwood et al.*, 2008]. Such HFAs, formed during the interaction with a TD in the solar wind and the quasi-parallel side of the Earth's bow shock, can generate considerable dynamic pressure fluctuations in the upstream solar wind and can have a significant impact on the magnetosphere [e.g., *Sibeck et al.*, 1999]. *Fairfield et al.* [1990] suggested that radial IMF, as well as solar wind dynamic pressure and IMF B_z dependence, also controls the location of the subsolar magnetopause via pressure fluctuations that originate in the convecting foreshock that is formed upstream of the quasi-parallel side of the bow shock. *Sibeck et al.* [2000] and *Omidi et al.* [2009] reported that the pressure increases bounding the cavity of the foreshock within which a fraction of solar wind ions reflected from the bow shock become suprathermalized due to instabilities, compress the magnetopause inward, whereas the decrease within the foreshock cavity allows it to expand outward.

[18] Note also that both the anti-sunward speed and the density of the solar wind (Figures 2d and 2h) (and therefore, the solar wind dynamic pressure and M_A, see Figures 2j and 2k) decrease across the IMF TD. The decrease in the density, dynamic pressure, and M_A is preceded by a transient (~10-minute long) enhancement. Figure 3 shows the results of an MHD simulation of this event using the BATS-R-US code. The simulation was run at the CCMC (Community Coordinated Modeling Center, http://ccmc.gsfc.nasa.gov). For four selected times around the TD arrival, the *xy*-plane (and *xz*-plane, not shown) cuts of the simulation domain along the Cluster trajectory show the expansion of the magnetosphere after the TD passes. The TD arrival at the bow shock results in an ~11-minute-long compression phase (Figure 3b) that is followed by an ~20-minute-long rarefaction phase. This slow rarefaction proceeds continuously until the end of the run (Figures 3c and 3d). The location of Cluster, marked by a red dot in each panel of Figure 3, is consistent with the observed forward-and then-backward Cluster traversal of the magnetopause, as was suggested from Figure 1.

[19] We conclude that both the variations in solar wind dynamic pressure around the arrival of, and across the

IMF TD (a transient increase, followed by the decrease; Figure 2j) and the kinetic processes associated with the formation of HFAs and/or foreshock cavities can account for a transient inward motion of the magnetopause, during which time both plasma and the magnetic field are compressed, followed by its outward motion during which time spacecraft in the dayside magnetosphere observe a rarefaction. The compression and rarefaction are also observed by GOES 8 and 10 in the inner magnetosphere (not shown). One should note the possibility that the radial IMF might be more important than the decrease in dynamic pressure in causing the expansion of the magnetopause. This possibility was investigated statistically by *Dušík et al.* [2010] who showed that radial IMF decreases the effectiveness of the solar wind dynamic pressure.

[20] When Cluster re-entered the boundary layer at ∼1623 UT (Figure 1) near the northern evening-side magnetopause, it again observed boundary disturbances as indicated by repeated observations of two sub-boundary regions of high (low) density and low (high) temperature with a large portion of low (high) energy populations. Characteristics of these fluctuations, e.g., the primary frequencies, changed across the TD. In sections 2.2 and 2.3, we focus on the modes and properties of the boundary fluctuations detected before and after the IMF TD. However, it should be noted that such differences might partially have been caused by spatial difference between the two times of the observations as Cluster was outbound toward the Sun during the entire ∼5-hour period of the event.

2.2. Identification of the Modes of the Boundary Fluctuations

[21] Pre-TD boundary fluctuations observed during 1200–1510 UT reveal the superposition of multiple frequencies, indicated by multiple periods embedded in the repeated patterns of the particle energy spectrograms (Figures 1b and 1d). The longest-period mode, which consistently involves intervals of increased plasma density (up to >4 cm^{-3}) is numbered in the sequence at the bottom of Figure 1b. Shorter period modes occur quasiperiodically during the ∼3-hour pre-TD period (e.g., note the periodic appearances of more-magnetosheath signatures between '4'–'5'). This coexistence of multiple (longer/shorter-period) modes are also found during 1623–1657 UT, i.e., in the post-TD period.

[22] The four Cluster spacecraft were in a tetrahedral configuration during this event. To identify the modes of these fluctuations, we employed the *k-filtering* technique, which provides an identification of the modes by estimating the distribution and localization of the magnetic field energy in (ω, **k**) space (see details in, e.g., *Sahraoui et al.* [2003]). The large spacecraft separation of ≥4,050 km during this event limits the identification of wave modes using k-filtering to relatively long-wavelengths, (e.g., within [d, 10d] where d is spacecraft separation [*Sahraoui et al.*, 2010].

[23] Figures 4b–4d and 4g–4i show the spectral power densities (SPD) of the magnetic field obtained from the Fluxgate Magnetometer (FGM) experiment [*Balogh et al.*, 2001] during the pre- and post-TD period, respectively. Figures 4b and 4g show the total (black), **l** (red, along the geomagnetic field), and combined (**m**, **n**) (green, perpendicular to the geomagnetic field) components of the spectral power densities. Here, we decomposed the magnetic field data onto the boundary normal coordinates, which vary in time and space, i.e., along the Cluster trajectory, using the magnetopause model of *Shue et al.* [1998]. The time-varying solar wind conditions during the event period that are obtained from ACE HRO data are used for the model. The spin-averaged magnetic field data (with ∼4-sec temporal resolution) were used both for this decomposition and the identification of low-frequency (< a few tens mHz) waves in this event.

[24] Figures 4c, 4d, 4h, and 4i show the **m**- and **n**-directional SPD, respectively. The **m**-directional SPD are expected to be most enhanced for the KHI mode. For both periods, the perpendicular components are significant, so the peaks of the total SPD are generally associated with the perpendicular, particularly the m-component SPD. We label the modes corresponding to these peaks as α, β, χ, δ, ϵ for the pre-TD period, and β', χ', δ', ϵ' for post-TD in the order of low-to-high frequencies. Note that the k-filtering technique applied to this event can resolve waves of ∼0.7–30 mHz frequency range, as estimated by an accessible range of $|k| = [0.1\ k_{max}, k_{max}]$ where $k_{max} = \pi/\langle d \rangle$ and $\langle d \rangle$ is average separation between the spacecraft [see *Sahraoui et al.*, 2010], and the phase velocities of the fluctuations obtained from the four-spacecraft timing as shown in Figures 5a–5f. The wave characteristics for each mode are detailed in Figures 4e and 4j for the pre- and post-TD periods, respectively.

[25] The (total) SPD of the lowest frequency mode during the pre-TD period, α, has contributions from the l-component (red curve in Figure 4b) and, less so, from the n-component (Figure 4d). This mode corresponds to the poloidal mode of the geomagnetic pulsation. Its period (∼21 min) is close to the period of the longest-period fluctuations marked by 1–6 in Figure 1b. The wave vector points toward the $-\mathbf{m}$ (and $-\mathbf{n}$) direction, i.e., along the direction perpendicular to the local magnetic field. This mode is directly correlated with solar wind dynamic pressure fluctuations (Figure 2j). Figures 4a and 4f show spectral densities of the solar wind dynamic pressure measured from wind at ∼3-sec resolution for pre- and post-TD periods, respectively. Note that the most distinctive peak in the solar wind dynamic pressure spectrum before the IMF-TD coincides with mode α. Such a link to the variations of the solar wind dynamic pressure is not present for higher-frequency modes ($\beta-\epsilon$). The mode α is absent for the post-TD period, during which time the lowest frequency mode is β', which has poor correlation with solar wind dynamic pressure.

[26] Higher frequency modes (β and χ before the TD and β' and χ' after the TD) are within the range of Pc5 (∼2–7 mHz) pulsations. The wave vectors of the pre-TD modes are oblique to the background geomagnetic field and show a significant -**l** and -**m**-directional propagation, i.e., toward the dusk equatorial plane. The post-TD modes are nearly perpendicular to the local magnetic field and mainly propagate either along the boundary normal (mode-β') or antiparallel to the normal direction (mode-χ').

[27] Even higher-frequency modes (δ and ϵ before the TD, and δ' and ϵ' after the TD) are within the frequency range of Pc4 (∼7–22 mHz) pulsations. Pre-TD modes are approximately perpendicular to the background magnetic field, while post-TD modes are oblique.

[28] Higher-frequency modes before the passage of the TD ($\beta-\epsilon$) have lower frequencies than the corresponding

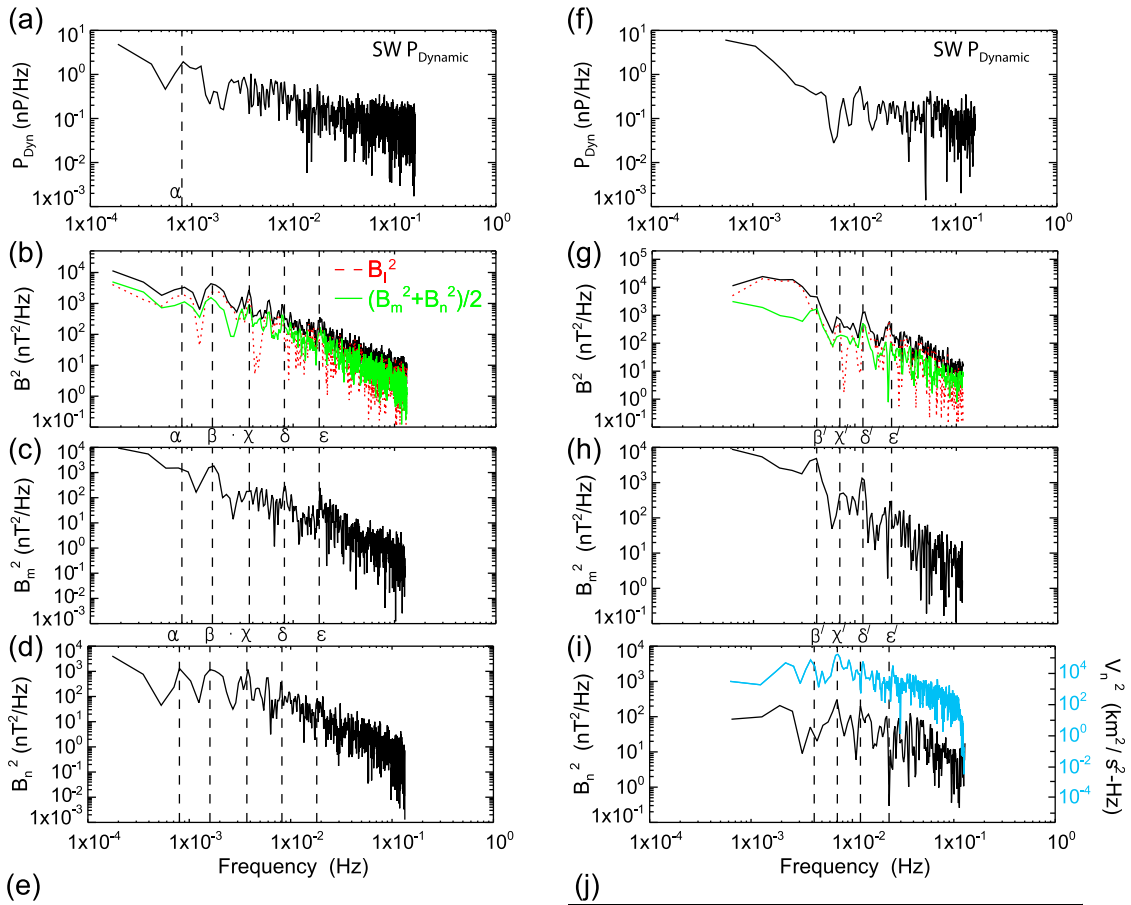

(e)

Mode	α	β	χ	δ	ε
Freq (Hz)	0.0008	0.0016	0.0037	0.0082	0.018
k in (**l**, m, n) coordinates	(0, -2, -1) /10⁴	(-8, -9, 7) /10⁴	(-10, -9, 5) /10⁴	(2, -9, 7) /10⁴	(3, -5, 10) /10⁴
Angle (**k**, **B**)	89°	124°	133°	79°	73°

(j)

Mode	β′	χ′	δ′	ε′
Freq (Hz)	0.0042	0.0071	0.012	0.023
k in (**l**, m, n) coordinates	(-3, -2, 10) /10⁴	(-2, -3, -11) /10⁴	(-4, 4, 2) /10⁴	(-8, 4, 6) /10⁴
Angle (**k**, **B**)	108°	101°	133°	139°

Figure 4. (a, f) The spectral densities of the solar wind dynamic pressure measured from Wind spacecraft at 3-sec resolution for (left) pre-TD and (right) post-TD periods, respectively. (b, c, d, g, h, i) The spectral power density for the magnetic field that are decomposed into [*l*, *m*, *n*] components using a magnetopause model. (Blue profiles in Figure 4i represent the power spectra of the V_n component.) (c, j) The results of k-filtering techniques applied for pre-TD and post-TD periods.

post-TD ($\beta' - \epsilon'$) fluctuations. We defer further discussions about the variations in frequency between the two periods to the following sections.

2.3. Propagation and Normals of the Boundary Fluctuations

[29] In this section we investigate the propagation of fluctuations at the boundary crossing between the more-magnetosheath and more-magnetospheric regions using the timings [*Paschmann and Daly*, 1998] of the four spacecraft observations of similar profiles among electron/ion density, electron/ion temperature, and electron characteristic energy (defined by the energy flux divided by the number flux—the black curve in Figure 1d). These profiles from the four Cluster spacecraft, however, show differences indicating variations of the waveforms across the boundary layer. We determine the timings using the time shifts that give the best correlations between the profiles from the different spacecraft [*Hwang et al.*, 2011] (see Appendix A).

[30] These boundary fluctuations (especially, the ones for the shorter period modes) are not always sufficiently clear to permit a four-spacecraft timing analysis. Figures 5a–5f summarize the propagation and normal signatures of the boundaries that are identifiable from all four spacecraft. Each column represents (a) the notation of each boundary crossing and the time detected at the C1 location, (b) the propagation speed ($|\mathbf{U}|$) of the boundary fluctuation, (c) its propagation direction ($\hat{\mathbf{U}}$) in GSE coordinates, (d) the boundary normal from magnetic field MVA after averaging over the spacecraft for which the medium-to-minimum eigenvalue ratio is greater than 3 ('local LMN'), (e) the angle between the propagation direction and the normal of the local-NML coordinates (θ_1, or $180° - \theta_{(\hat{\mathbf{U}}, \mathbf{n}_{\text{local}})}$ if $\theta_{(\hat{\mathbf{U}}, \mathbf{n}_{\text{local}})} > 90°$), and (f) the angle between the nominal (averaged) normal and the local normal (θ_2). Both θ_1 and θ_2 lie within [0°, 90°]. Here, the averaged boundary normals ('ave LMN') are obtained from MVA of the low-pass filtered magnetic

(a) Boundary X-ing time	(b) $\|U_{prop}\|$	(c) $\hat{U}_{prop}$ $(x, y, z)_{GSE}$			(d) Local normal from MVA $(n_{local})_{GSE}$			(e) θ_1 $(\hat{U}_{prop}, n_{local})$	(f) θ_2 (n_{model}, n_{local})
1 12:32:46	103.1	-0.904	-0.330	0.270	0.951	-0.147	-0.270	27.8	21.6
1 HF 12:45:03	113.8	-0.876	0.012	-0.483	0.955	-0.011	0.297	46.3	36.9
2 13:00:55	50.6	-0.116	-0.435	-0.893	-0.452	0.808	0.377	50.5	48.3
2 HF 13:11:23	75.6	-0.953	0.224	0.204	0.681	0.590	-0.434	57.2	41.5
3 13:32:48	45.5	-0.980	-0.190	-0.065	0.966	-0.253	0.052	25.7	15.3
3 HF 13:49:20	35.2	-0.465	0.592	-0.659	0.868	-0.372	0.330	66.4	28.4
4 13:51:42	41.8	-0.960	0.119	-0.254	0.810	-0.583	0.064	30.3	24.5
5 14:14:20	46.7	-0.995	0.027	-0.098	0.932	0.229	0.280	18.4	24.9
6 14:41:29	35.9	-0.809	-0.375	-0.453	0.930	0.248	0.270	14.6	26.5
MP 1st –X 15:10:09	123.0	-0.926	0.111	-0.360	0.963	0.178	0.203	19.1	23.6
MP 2nd-X 16:26:59	18.6	-0.871	-0.426	-0.246	0.717	0.249	0.651	27.1	27.7
Post-TD 1 16:39:25	83.8	-0.459	0.808	0.369	0.565	0.523	0.638	66.5	16.4
Post-TD 2 16:41:16	63.1	-0.824	-0.430	-0.370	0.003	0.983	0.185	60.8	50.5
Post-TD 3 16:48:42	209.0	-0.518	0.617	0.592	0.998	-0.057	0.017	57.2	27.1

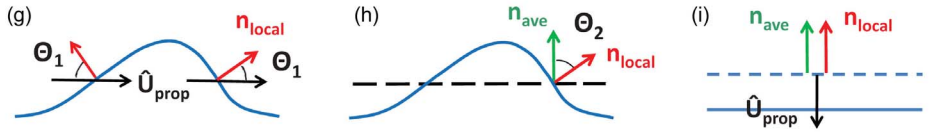

Figure 5. (a–f) Properties of the boundary fluctuations. Fluctuations, denoted by red (black) letters, meet (do not meet) the KHI criterion across corresponding boundary crossings (see the details in the text). (g–i) The angles representing the steepness of the disturbed wavefront.

field (to remove fluctuating signatures) around each boundary crossing. We require that the medium-to-minimum eigenvalue ratio is greater than 2. These angles indicate the steepness, or degree of disturbance of locally fluctuating boundary surfaces relative to the undisturbed magnetopause boundary: When θ_1 (θ_2) becomes smaller, the steepness of the waveform is larger (smaller) (see Figures 5g and 5h).

[31] We denote the longest-period signatures by numbers, 1–6 (as marked in Figure 1b), and the shorter-period signatures as a number designated for the longest-period mode that occurred prior to the shorter-period mode, followed by 'HF,' (e.g., 1 HF, 2 HF, and 3 HF in Figures 5a–5f). The first and second entry to the magnetopause ('MP 1st -X' and 'MP 2nd-X') are at ~1510:09 UT and ~16:26:59 UT, respectively. During the second magnetopause crossing, boundary fluctuations observed coherently among the four spacecraft are labeled 'Post-TD 1–3' in Figure 5a.

[32] The longest-period fluctuations, 1–6 in Figure 5a show a predominantly anti-sunward propagation along $-\mathbf{x}$ (except for fluctuation-2, which propagates mainly along $-\mathbf{z}$). Boundary normals of these fluctuations generally align with their propagation directions, making θ_1 less than ~30° (Figure 5e). This either indicates a highly steepened waveform of local fluctuations (Figure 5g), or a global motion of the boundary, which is assumed to be planar over the spacecraft separation (Figure 5i). For the former, the smaller θ_1 is expected to correspond to the larger θ_2 (Figure 5h) because the sum of the two angles is ideally 90° for a waveform moving along the boundary. On the other hand, for the latter θ_2 is expected to also be small. Figures 5e and 5f demonstrate that the latter can generally explain fluctuations 1–6.

[33] For example, Figure 6 shows the relative location of the four spacecraft around their barycenter in the *xz*, *xy*, and *yz* planes at the times of fluctuation-'6' near 14:41:29 UT. The thick gray arrows represent the projections of the derived propagation velocity of the boundary fluctuation, and the magenta arrow at each spacecraft shows the normal direction of the boundary associated with fluctuation-'6'. The lengths of the velocity vectors shown at the upper right corner in the first panel correspond to a propagation speed of 25 km/s (grey). The boundary normals are consistent among the four spacecraft and they relatively align with the propagation direction, which is mostly along the anti-sunward (and dawnward/equatorward) direction, corresponding to the inward motion of the global boundary (for the stationary

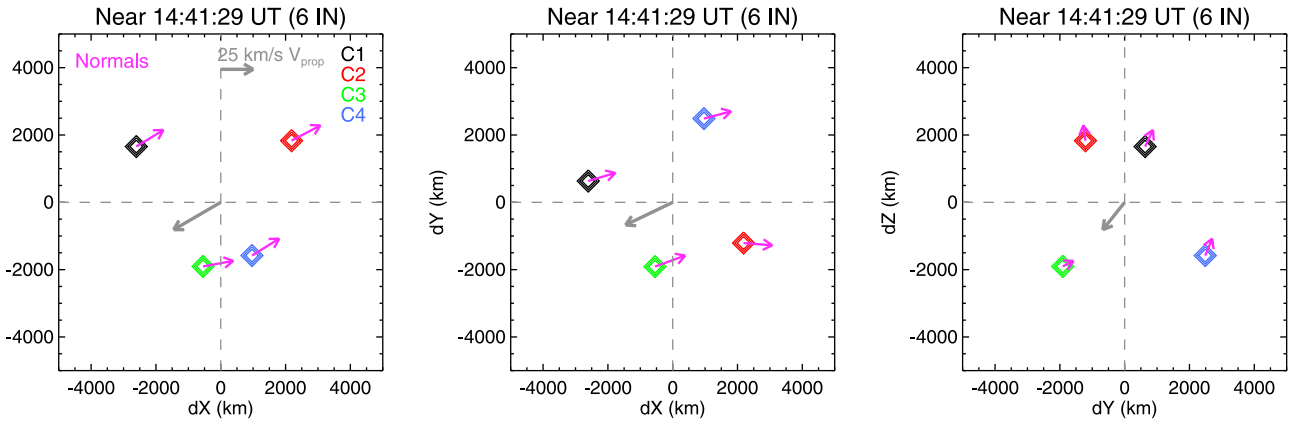

Figure 6. The relative location of the four spacecraft around their barycenter in the *xz*, *xy*, and *yz* planes at the times of '6 IN' observations near 14:41:29 UT (see the details in the text).

spacecraft to observe the more-magnetospheric region, and then immediately, more-magnetosheath region). Therefore, the longest-period fluctuations are likely to represent repeated inward disturbances of the dayside magnetopause associated with the solar wind dynamic pressure variations. This is consistent with our conclusion for mode α in Figure 4 (left) and the discussion in section 2.2.

[34] We applied the KH instability condition (equation 1) for the periods adjacent to each boundary crossing. The reference points from the magnetosheath and magnetospheric sides around each boundary were selected as 3–7 (mostly averaged) spin periods (corresponding to 12–28 s) before and after each boundary crossing so that they were neither adjacent to the boundaries nor embedded deeply inside a region. This was done to ensure that the data were obtained near the interface of two velocity layers that are assumed to constitute a zero-thickness interface in equation (1), while excluding any microscopic physical processes occurring at the boundaries.

[35] Fluctuations, 1, and 3–6, denoted by red text in Figures 5a–5f, meet the KHI criterion. The KH-unstable condition is not commonly satisfied at the high-latitude cusp region mainly because the intense geomagnetic field (compared to the magnetic field in the LLBL/flanks of the magnetopause) stabilizes the KHI mode. However, when considering a dominant $-y$-component of the IMF (Figure 2a) and the observation location near the northern dusk cusp (also having a dominant $-y$-component of the geomagnetic field), the magnetic fields in the magnetosheath and magnetosphere near the boundary layer are almost parallel. The anti-sunward wave vectors shown in Figure 5c reduce the right-hand term of equation (1), although the velocity shear (200 km/s on average) is half that at the LLBL/flanks (as speculated from the solar wind speed of ~400 km/s for this event).

[36] The propagation and normal properties of the shorter-period boundary fluctuations ('1–3 HF') reveal two findings: (1) They mainly propagate tailward, but with a significant diversion either duskward or southward (toward the equatorial plane). (2) The sums of θ_1 and θ_2 are close to 90°, indicating that these fluctuations constitute local boundary fluctuations. These higher-frequency-mode boundary fluctuations do not necessarily meet the KHI criterion: '1 HF' and '3 HF' do not meet the KHI condition, while '2 HF' does. However, one should note that satisfying the KHI condition does not necessarily imply that the observed fluctuations are KHW: it only indicates (1) whether or not the observed waves are currently stable or unstable to the KHI, or (2) if they are KHW, whether or not they are undergoing nonlinear evolution.

[37] Cluster crossed the magnetopause twice: The initial entry to the magnetopause ('MP 1st-X'), resulted from the transient compression of the dayside magnetosphere associated with the arrival of the IMF-TD, occurred at ~1510:09 UT, and the second crossing denoted 'MP 2nd-X' was outbound at ~16:26:59 UT. The magnetopause was unstable to the KHI during the first entry (MP 1st-X).

[38] Post-TD boundary fluctuations, 'Post-TD 1–3' in Figure 5a, are observed after the IMF TD convected to the tailward magnetosphere. They predominantly propagate tailward, but their normal directions and waveform steepness vary considerably. The sum of θ_1 and θ_2 is, however, close to 90°, indicating that they are local perturbations. During this post-TD period, the boundary signatures are often very different over the four spacecraft, making a timing analysis difficult or impossible. This suggests either that the boundary disturbances have scales smaller than the spacecraft separation, or that the wave properties are highly variable in space and/or in time.

[39] We expand this interval in Figure 7. Figure 7a shows the magnetic field in the boundary normal coordinates that are obtained from using the *Shue et al.*'s [1998] model along the Cluster trajectory for the time-varying solar wind inputs. The magnetic field variations (a bipolar B_n and/or a peaked B_m) in the boundary coordinates around the magenta vertical lines often coincide with the increases in the plasma density/pressure and/or magnetic pressure. This suggests that Flux Transfer Event (FTE) structures are present, in which case the observed post-TD boundary fluctuations are associated with the passage of a series of FTEs drifting along the dayside magnetopause. Under sunward IMF during this post-TD period, the region of largest magnetic shear is near the high-latitude subsolar magnetopause where the convecting flux ropes can form. The convection of FTEs can explain the polarity of the B_n variation across the magenta lines: a negative-to-positive B_n at ~1641:12 UT in Figure 7a corresponds to the southward (and dawnward) propagation of

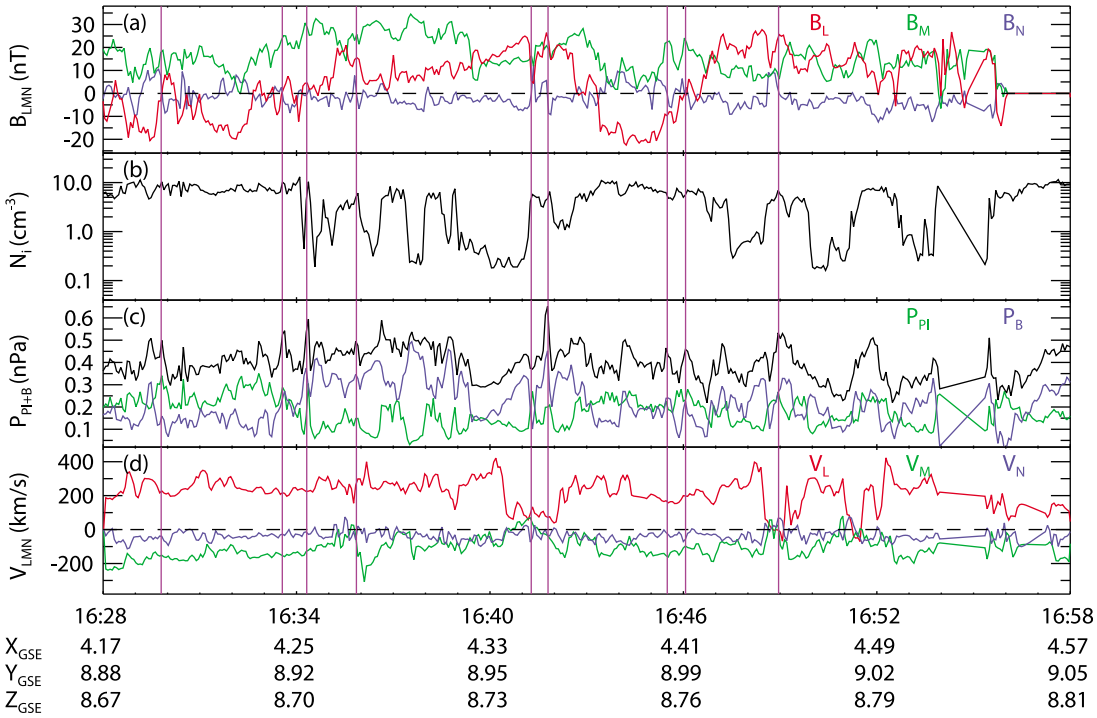

Figure 7. After the IMF-TD observations: (a) the *l* (red), *m* (green), and *n* (blue) component of the magnetic field; (b) the ion density; (c) the total (black), plasma (green), and magnetic (blue) pressure; (d) the ion velocity along the *l* (red), *m* (green), and *n* (blue) direction. Magenta vertical lines represent the timings when FTE signatures are observed.

fluctuation-'Post-TD 2', and a positive-to-negative variation of B_n at ~1649 UT can explain the northward (and duskward) propagation of fluctuation-'Post-TD 3'.

[40] There are, however, several caveats in interpreting the post-TD fluctuations as a series of FTEs past the spacecraft: 1. In general, dayside FTEs are unlikely to emerge during radial IMF (although the FTE occurrence is higher during sunward IMF than during antisunward IMF [*Wang et al.*, 2006]). 2. The bipolar-B_n signatures (Figure 7a) are not prominent in comparison with the magnetic field variations in other directions and are buried in a background of fluctuations with similar magnitudes and durations. This indicates that the bipolar-B_n structures have been superposed on the boundary that contained other fluctuations. 3. Such atypical fluctuations are easily generated near the magnetopause from variations in solar wind parameters.

[41] Related to 2, we, in particular, note a series of KHW-like patterns during 1636–1639 UT and 1647–1653 UT in Figure 7: When the density is low, magnetic (plasma) pressure is high (low) and bulk plasma velocity either along or normal to the boundary is negative, suggesting a series of magnetospheric-side plasmas flowing duskward and tailward. These periodic variations indicate the occurrence of KHW. Typical periods of these repeated signatures correspond to modes β' and χ' (Figure 4, right). Signatures of KHW often tend to be seen in variations of the *n*-component of flow velocities. Indeed, the power spectra of the V_n component shown as blue in Figure 4j, show enhancements at these two frequencies, corresponding to modes β' and χ', showing a good correspondence with the B_n spectra. These arguments support the conclusion that the observed boundary fluctuations during the post-TD period are likely to be KHW than FTEs. We defer further discussions about the relationship between KHW and FTEs in the following section.

3. Discussion

[42] The boundary layer near the cusp region is a region where a high level of turbulence and abundant waves are often present. The most likely source of these waves, ranging up to a few hundreds of Hz (for electromagnetic waves) or a few thousands of Hz (for electrostatic), is dayside magnetic reconnection [e.g., *Pickett et al.*, 2001]. One might argue that a quasiperiodic appearance of high-energy particles (Figures 1b and 1d) can be interpreted as being generated by bursty dayside reconnection with a quasiperiodic reconnection rate. However, the present event of boundary fluctuations with frequencies below a few tens of mHz are observed when dayside reconnection is not favored. Furthermore, the periods of Cluster's excursion into the inner boundary layer (more-magnetospheric region) that shows a higher portion of high-energy populations both before and after the IMF TD (black triangles in Figure 1b mark some of those timings) corresponds to the periods of reduced plasma bulk velocity (Figure 1h), indicating that the particles are pre-existing plasma of magnetospheric origin, rather than the injected population produced by reconnection. For the post-TD period, we suggested a possibility that the Cluster observations represent boundary fluctuations resulting from the passage of FTEs. It is, however, debatable if such periodic reconnection to explain a periodicity in the observed

after-TD signatures is plausible during this period, especially in light of caveats 1–3 in section 2.3.

[43] The notable duration (~3-hour and 34-minute for the pre- and post-TD periods, respectively) and the relatively wide extents of this event imply that the observed plasma and field signatures are global fluctuations of the magnetopause. In contrast to most cusp-region turbulent waves, the present event is also characterized by simultaneous variations of particle signatures in accordance with those of the magnetic field: Both before and after the passage of the IMF discontinuity, the regions of depressed magnetic field (the outer boundary layer, or more-magnetosheath region) are consistent with the observations of abundant low-energy particles, high density, and low temperature of plasma. The regions of enhanced magnetic field (the inner boundary layer, or more-magnetospheric region) are coincident with high energy particles, low density, and high temperature. These are typical signatures of KHW observed in the boundary layer adjacent to the Earth's magnetopause. This is further supported by the fact that the bulk velocity of the plasma and the magnetic field between the two sub-boundary regions often satisfy the KH-unstable condition in this event.

[44] These arguments support the conclusion that this event represents the first in situ observation of high-latitude (near the northern post-noon cusp) KHW under strongly dawnward IMF. The dayside near-cusp magnetopause is rarely unstable to the KHI mainly because to the intense geomagnetic field (compared to that in the LLBL). Even though the magnetic fields in the two velocity-shear, sub-boundary layers are either parallel or antiparallel, if the wave vector points significantly away from the direction perpendicular to the two magnetic fields, large magnitudes of those magnetic fields easily increase the right-hand term of equation (1), resulting in the suppression of the generation of KHI.

[45] In the present event, the KHW-unstable fluctuations propagate predominantly tailward. As a result, the wave propagation vector is almost 90° to both the magnetosheath and geomagnetic fields, which lowers the threshold of the KHI. The magnetic configuration across the boundary layer near the northern duskward cusp region during the dawnward IMF orientation is similar to that in the dayside LLBL, or flank magnetopause under northward IMF, in that (1) the magnetosheath and magnetospheric fields across the local boundary layer constitute the lowest magnetic shear, and (2) the tailward propagation of the KHW is perpendicular to both fields (see Figure 8a). Since the IMF with the Parker spiral topology usually have predominant x- and y-components, KHW generated at high latitudes may play an important role in particle and momentum transfer from the solar wind to the magnetosphere, especially when the wave vector is oriented to favor growth of the KHI.

[46] The boundary fluctuations continued for more than three hours before the arrival of the IMF discontinuity with its rapid dawnward-to-sunward change of the IMF orientation. When Cluster re-entered the post-noon magnetopause, the spacecraft observed fluctuations on the boundary layer that differed in character from those observed before the TD passed the spacecraft.

[47] The summary of these wave modes and illustration of their propagations are shown in Figure 8. The lowest-frequency mode (mode-α or fluctuations 1–6) during the pre-TD period corresponds to a global inward motion of the dayside magnetopause, rather than a local fluctuation, while higher-frequency modes before the TD (modes $\beta-\epsilon$ or fluctuations 1–3 HF) and after the TD (modes $\beta'-\epsilon'$ or 'Post-TD 1–3') represent local boundary perturbations. The lowest-frequency fluctuations propagate mostly tailward, and are found to be unstable to the KHI. They show a direct correlation with the solar wind dynamic-pressure impulses, which indicates that the observed anti-sunward motion of the lowest-frequency mode is caused by transiently enhanced solar wind dynamic pressure. This also implies that the variations of the solar wind dynamic pressure have acted as a seed fluctuation for the generation of the KHW (higher-frequency modes) in this event.

[48] Higher-frequency modes ($\beta-\epsilon$, $\beta'-\epsilon'$) lie within the range of Pc4 or Pc5 pulsations. Local boundary fluctuations corresponding to the pre-TD higher-frequency modes slightly divert duskward and southward from their dominantly tailward propagations. *Farrugia et al.* [1998] delineated the KH-unstable band on the surface of the magnetopause as the regions of low magnetic shear between the magnetosheath and geomagnetic fields for tailward wave propagation, especially behind the dawn-dusk terminator. Such considerations predict that the KH-unstable band emanates from the cusp and broaden as it approaches the equatorial plane [see *Farrugia et al.*, 1998, Figure 1]. The derived propagation directions of the pre-TD high-frequency modes presented here, therefore, suggest that they appear to orient themselves so that they become most-unstable to the KHI (Figure 8a).

[49] Boundary fluctuations representing the post-TD higher-frequency modes show less coherence in wave properties (normal and steepness of the waveform), except for their periodicity and primarily tailward propagation. The field variations in the boundary coordinates and simultaneous observations of the peaks in plasma density/pressure or magnetic pressure suggest a possibility that they are associated with the passages of a series of FTE structures drifting along the magnetopause. In fact, the relationship between the KHW and FTEs has long been investigated: KHW can generate FTEs and visa versa [*Russell and Elphic*, 1978; *Sckopke et al.*, 1981; *Nakamura et al.*, 2008; *Nakamura and Fujimoto*, 2008], and/or the two are sometimes simultaneously observed [*Eriksson et al.*, 2009; *Hwang et al.*, 2011]. The FTEs that have been generated near the subsolar location and that drift along the magnetopause to the magnetotail, can also disrupt the previously formed KHW/KHV [*Kuznetsova et al.*, 2008]. Our analyses and the aforementioned caveats in the FTE interpretation (section 2.3) demonstrate that the observed bipolar-B_n structures during the post-TD period are embedded within other background fluctuations that are most likely to be KHW. Such FTEs would only superpose small perturbations on the primary fluctuations, resulting in the observed incoherence in the wave properties among the post-TD boundary fluctuations. Therefore, following discussions are based on that both the pre- and post-TD magnetopause fluctuations represent KH modes.

[50] The frequencies of the higher-frequency modes increase after the IMF-TD passage. *Miura and Pritchett* [1982] found that the wavelength of the fastest growing KH mode is proportional to the initial thickness of the velocity shear layer. On the other hand, *Farrugia et al.* [1998, 2003]

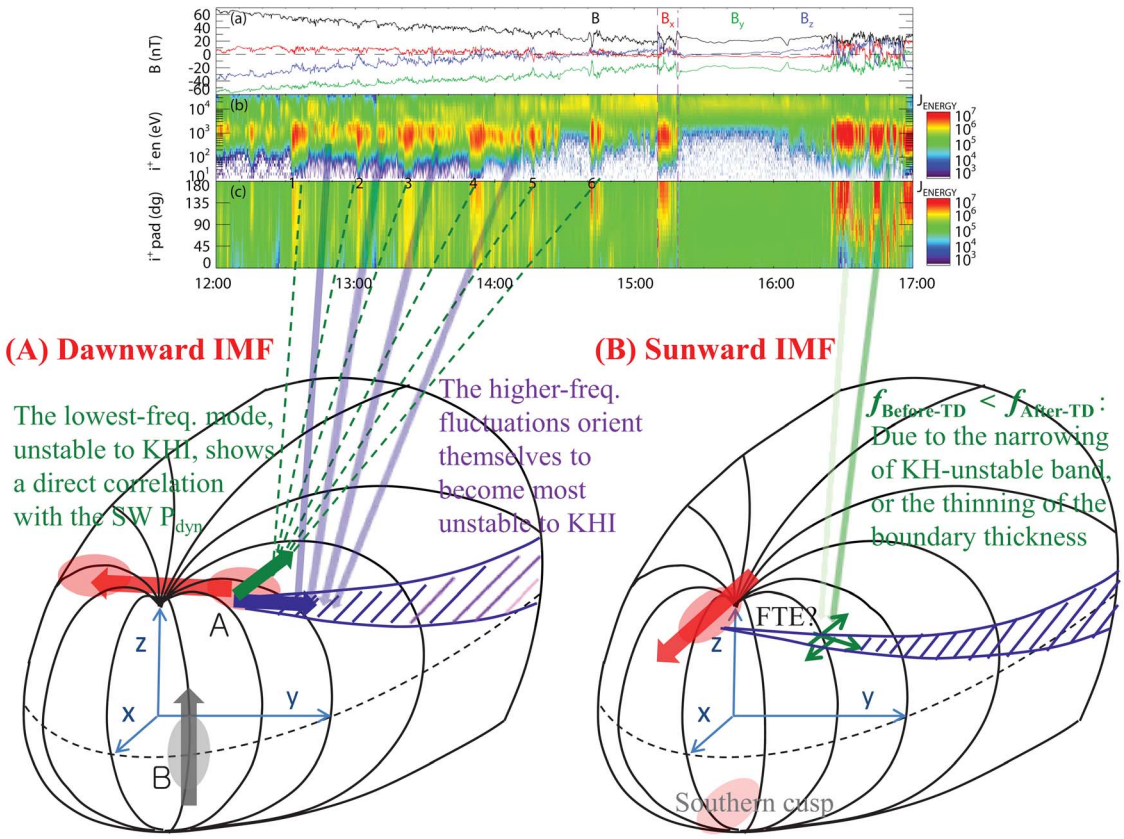

Figure 8. Illustrations of topologies of the Earth's magnetopause during (a) dawnward and (b) radial IMF (thick red arrows) conditions. Parallel and anti-parallel orientations between the magnetosheath and magnetospheric fields are shown as a red shade. A slashed region indicates the KH-unstable band on the surface of the magnetopause, as speculated by the regions of low magnetic shear between the two fields and consideration of a predominant tailward wave propagation behind the dawn-dusk terminator. The derived propagations of the boundary fluctuations for each mode are marked by green (the lowest-frequency mode before the IMF-TD), blue (higher-frequency mode before the TD), and green (during the post-TD period) arrows. Figures 1a–1c at the top are shown as references to correlate these wave modes in the Cluster observations. Note that related to the KHW generation, magnetic configuration between the magnetosheath and magnetosphere at Figure 8a under dawnward IMF conditions is similar to that at Figure 8b under northward IMF in that these areas are the regions of the lowest magnetic shear between the magnetosheath and the dayside magnetopause.

reported that the width of the KH-unstable bands on the surface of the magnetopause controls the wavelength of the KHW that can be generated for a given IMF clock angle. Based on these studies, the observed frequency increase, or wavelength decrease across the IMF TD passage implies either thinning of the boundary layer, or a narrowing of the KH-unstable band on the dayside magnetopause.

[51] The change in the thickness of the boundary layer can arise from (1) a thinning of the magnetopause generally along the sunward direction (and therefore, in this case, we are observing a spatial effect caused by the translocation of the observation point along the Cluster's outbound trajectory), and/or, (2) a consequence of the sunward orientation of the IMF, causing the magnetic shear across the northern subsolar magnetopause to become larger, which, in turn, causes a thinning of the boundary layer. The largest spacecraft separation along the boundary normal (time-varying **n** obtained from the *Shue et al.* [1998] model) changed from ~5,450 to ~4,370 km during the pre-TD, and from ~3,760 to ~3,720 km after the TD. If we assume that the spacecraft separation is indicative of the thickness of the boundary layer (because coherently fluctuating boundary signatures among the four spacecraft are marginally observed during both periods), then the wavelengths of the fastest-growing KH mode will be ~6.42–5.14 R_E before the IMF-TD and ~4.43–4.38 R_E after it. (Here, we used the *Miura and Pritchett* [1982] formula, $15/2 \times D \approx \lambda_{Max.growth}$ where D and $\lambda_{Max.growth}$ represent the thickness of the initial velocity shear layer and the wavelength of the most unstable KH mode, respectively.) The estimated wavelengths are relatively smaller than those of KHW detected at the flank of the magnetopause near the dawn-dusk terminator [e.g., *Fairfield et al.*, 2007; *Hasegawa et al.*, 2004], which indicates a consistency with the argument that the wavelength of KHW is smaller on the higher latitude magnetopause than lower latitudes [*Farrugia et al.*, 1998]. Using the propagation velocities of boundary fluctuations derived using four-spacecraft timing analysis (Figures 5a–5f), the frequency of the fastest-growing

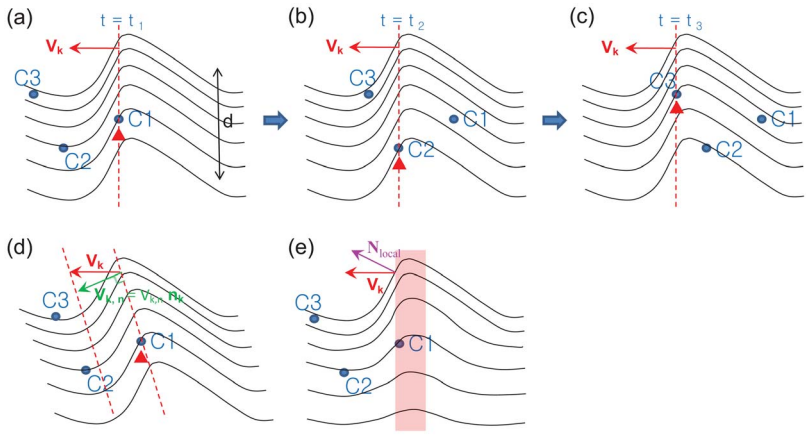

Figure A1. Two-dimensional illustration of a fluctuating boundary layer with a thickness, *d*. Identical waveforms across the boundary, denoted isosurfaces, propagate to the left with a velocity, $\mathbf{V_k}$. A red dotted line represents a line which connects the same phase among these isosurfaces, i.e., the wavefront (a–c). (d) and (e) depict more general cases where the wavefront is not necessarily perpendicular to the wave propagation (d), and where the waveforms show certain variations across the boundary layer (e). See the text for more details.

KH mode ranges within 1.10–2.85 mHz before the IMF-TD to 2.24–7.49 mHz after it. These frequencies correspond to mode β before the IMF-TD and modes $\beta'-\chi'$ after it (see Figures 4e and 4j). In fact, there is a linear relationship between pre-TD and post-TD frequencies, $f_{\text{post-TD}} \sim 2.65 \times f_{\text{pre-TD}}$, which corresponds to the estimated decreases in wavelength and/or thickness of the magnetopause boundary.

[52] A narrowing of the width of the KH-unstable bands on the dayside magnetopause is also expected from the behavior of the dayside magnetopause under a rapid change of the IMF cone angle. The duskward near-cusp magnetopause in the northern hemisphere during the dawnward IMF constitutes a broader KH-unstable band than under the sunward IMF, during which time the high-latitude subsolar magnetopause has low magnetic shear with a narrow width (compare Figures 8a and 8b). Therefore, both thinning of the boundary thickness, or a narrowing of the KH-unstable band on the surface of the dayside magnetopause (associated with the dawnward-to-sunward IMF orientation) can explain the frequency increase of the higher-frequency KH modes between the pre- and post-TD intervals.

[53] The present study first demonstrated an occurrence of KHW in the northern duskward cusp region. We have found that the properties of KHW appear to change depending on the orientation of the IMF. Our results suggest the need for further study of the generation and development of KHW under a variety of IMF orientations.

Appendix A: Estimating the Propagation Velocity of the Wavefront of the Boundary Fluctuations or the KH Mode

[54] To estimate the propagation velocity of the wavefront, i.e., the phase speed, $\mathbf{V_k}$ we first adopt the common idea that the boundary layer between the magnetosheath and the magnetosphere has a certain thickness along the boundary normal. As pointed out by *Foullon et al.* [2010, hereinafter F10], such geometry needs to be treated differently from the case of a two-dimensional boundary that is planar over the spacecraft separations (such as a planar shock). Despite the fact that the four-spacecraft timing analysis [*Paschmann and Daly*, 1998] is used under the assumption of plane-surface hypothesis, we show in this appendix that the timing analysis technique can be applied to estimate the propagation of fluctuations of the boundary layer having a certain thickness (contrary to F10), using the same isosurface idea assumed by F10.

[55] Figure A1 shows a two-dimensional illustration of arbitrary waveforms of surface fluctuations that maintain a coherency over the boundary thickness, *d*. We call these coherent waveforms *isosurfaces*, following F10. Without a loss of generality, we assume that three spacecraft (C1-3) form a triangular configuration onto such isosurfaces. (Note that the spacecraft separation is large enough that the three spacecraft can observe different isosurfaces.) A red dotted line represents a line which connects the same phase among these isosurfaces, i.e., the wavefront. A specific feature of the waveform (a *certain phase*) is often taken as a reference to read timings of the observation among the spacecraft. Once such a specific phase is uniquely observed between adjacent waveforms, the spacecraft read detection timings of the same wavefront (marked by a red dashed line in Figures A1a–A1c) at $t = t_1$, t_2, and t_3 by C1, C2,and C3, consecutively. This gives a pair of equations to derive the normal propagation of the phase speed, $\mathbf{V}_k$:

$$\mathbf{n_k}\cdot(\mathbf{r}_2 - \mathbf{r}_1) = V_{k,n}(\mathbf{t}_2 - \mathbf{t}_1)$$
$$\mathbf{n_k}\cdot(\mathbf{r}_3 - \mathbf{r}_1) = V_{k,n}(\mathbf{t}_3 - \mathbf{t}_1)$$

Here, $\mathbf{n_k} = (\mathbf{n_{k,x}}, \mathbf{n_{k,y}})$ and $V_{k,n}$ represent the unit vector and the magnitude of the normal propagation of the wavefront, respectively. (See Figure A1d, which illustrates a more general case where the wavefront is not perpendicular to the wave propagation.) $\mathbf{r_1}$, $\mathbf{r_2}$ and, $\mathbf{r_3}$ are two-dimensional vectors representing the location of each probe, C1, C2, and C3. A constraint, $n_{k,x}^2 + n_{k,y}^2 = 1$ completes a third equation to solve three unknowns of the normal propagation of the wavefront. The three-dimensional analysis using four

spacecraft is the same as this two-dimensional version. The *normal* wavefront velocity often aligns with the phase velocity as indicated by *Hwang et al.* [2011], which is the case for Figures A1a–A1c.

[56] Here, we point out that since a specific phase among isosurfaces provides a reference for a four-spacecraft timing, the timing analysis yields the propagation velocity of a *two-dimensional, planar* wavefront (not a curved waveform), which is defined by that specific phase among isosurfaces. Therefore, the derived propagation is ideally the normal velocity of the wavefront propagation, and it represents/approximates the phase velocity of the boundary waves [*Hwang et al.*, 2011].Note that in this case the derived normal propagation of the wavefront using this method and the local normal of the waveform (a magenta arrow in Figure A1e) do not have to be aligned with each other (as is required for a planar boundary). The angle between the wavefront propagation and the local normal of the waveform, instead, gives information about the steepness of the waveform (see θ_1 in Figure 5g and section 2.3).

[57] We expand this idea for more general geometry where the waveforms are not exactly identical across the boundary layer (Figure A1e). In this case, finding certain specific patterns in the waveform, i.e., a reference for the four-spacecraft timing becomes ambiguous. For the presented event, the fields and/or plasma profiles from the four spacecraft show variations among them, i.e., certain variations in the (almost-) isosurfaces across the boundary layer. Therefore, in this paper we determined timings using the time shifts that give the best correlations between the profiles measured by the four spacecraft [*Hwang et al.*, 2011], instead of using the timings that show any specific features in those profiles. We believe that this method can derive the propagation velocity of the waveform most accurately under given data sets.

[58] **Acknowledgments.** This study was supported by NASA's Cluster mission, by a Magnetospheric Multiscale Interdisciplinary Science grant at the Goddard Space Flight Center, and by Goddard grant 67394324/NCC5-494 to the UMBC/GEST program. We acknowledge all Cluster instrument teams, including PEACE, CIS, and FGM staffs and the Cluster Active Archive (http://caa.estec.esa.int/caa) from which all the processed science-level data were downloaded. Simulation results have been provided by the Community Coordinated Modeling Center at Goddard Space Flight Center through their public Runs on Request system (http://ccmc.gsfc.nasa.gov). We appreciate both reviewers' helpful comments and suggestions.

[59] Philippa Browning thanks the reviewers for their assistance in evaluating the paper.

References

Balogh, A. C., et al. (2001), The Cluster magnetic field investigation: Overview of in-flight performance and initial results, *Ann. Geophys.*, *19*, 1207–1217.

Burgess, D. (1989), On the effect of a tangential discontinuity on ions specularly reflected at an oblique shock, *J. Geophys. Res.*, *94*, 472–478, doi:10.1029/JA094iA01p00472.

Chandrasekhar, S. (1961), *Hydrodynamic and Hydromagnetic Stability*, Clarendon Press, Oxford, U. K.

Chen, Q., A. Otto, and L. C. Lee (1997), Tearing instability, Kelvin-Helmholtz instability, and magnetic reconnection, *J. Geophys. Res.*, *102*(A1), 151–161, doi:10.1029/96JA03144.

Chen, S.-H. and M. G. Kivelson (1993), On nonsinusoidal waves at the Earth's magnetopause, *Geophys. Res. Lett.*, *20*(23), 2699–2702, doi:10.1029/93GL02622.

Chen, S.-H., M. G. Kivelson, J. T. Gosling, R. J. Walker, and A. J. Lazarus (1993), Anomalous aspects of magnetosheath flow and of the shape and oscillations of the magnetopause during an interval of strongly northward interplanetary magnetic field, *J. Geophys. Res.*, *98*(A4), 5727–5742, doi:10.1029/92JA02263.

Claudepierre, S. G., S. R. Elkington, and M. Wiltberger (2008), Solar wind driving of magnetospheric ULF waves: Pulsations driven by velocity shear at the magnetopause, *J. Geophys. Res.*, *113*, A05218, doi:10.1029/2007JA012890.

Contin, J. E., F. T. Gratton, and C. J. Farrugia (2003), Theoretical results on the latitude dependence of the Kelvin-Helmholtz instability at the dayside magnetopause for northward interplanetary magnetic fields, *J. Geophys. Res.*, *108*(A6), 1227, doi:10.1029/2002JA009319.

Dungey, J. W. (1954), Electrodynamics of the outer atmosphere, in *Physics of the Ionosphere: Report of the Conference Held at the Cavendish Laboratory, Cambridge, September*, pp. 229–236, Phys. Soc. London, London.

Dušík, Š., G. Granko, J. Šafránková, Z. Němeček, and K. Jelínek (2010), IMF cone angle control of the magnetopause location: Statistical study, *Geophys. Res. Lett.*, *37*, L19103, doi:10.1029/2010GL044965.

Eastwood, J. P., et al. (2008), THEMIS observations of a hot flow anomaly: Solar wind, magnetosheath, and ground-based measurements, *Geophys. Res. Lett.*, *35*, L17S03, doi:10.1029/2008GL033475.

Eriksson, S., et al. (2009), Magnetic island formation between large-scale flow vortices at an undulating postnoon magnetopause for northward interplanetary magnetic field, *J. Geophys. Res.*, *114*, A00C17, doi:10.1029/2008JA013505. [Printed *115*(A1), 2010].

Fairfield, D. H., W. Baumjohann, G. Paschmann, H. Luehr, and D. G. Sibeck (1990), Upstream pressure variations associated with the bow shock and their effects on the magnetosphere, *J. Geophys. Res.*, *78*, 3731–3744.

Fairfield, D. H., A. Otto, T. Mukai, S. Kokubun, R. P. Lepping, J. T. Steinberg, A. J. Lazarus, and T. Yamamoto (2000), Geotail observations of the Kelvin-Helmholtz instability at the equatorial magnetotail boundary for parallel northward fields, *J. Geophys. Res.*, *105*(A9), 21,159–21,173, doi:10.1029/1999JA000316.

Fairfield, D. H., M. M. Kuznetsova, T. Mukai, T. Nagai, T. I. Gombosi, and A. J. Ridley (2007), Waves on the dusk flank boundary layer during very northward interplanetary magnetic field conditions: Observations and simulation, *J. Geophys. Res.*, *112*, A08206, doi:10.1029/2006JA012052.

Farris, M. H., and C. T. Russell (1994), Determining the standoff distance of the bow shock: Mach number dependence and use of models, *J. Geophys. Res.*, *99*, 17,681–17,689.

Farrugia, C. J., F. T. Gratton, L. Bender, H. K. Biermat, N. V. Erkaev, J. M. Quinn, R. B. Torbert, and V. Dennisenko (1998), Charts of joint Kelvin-Helmholtz and Rayleigh-Taylor instabilities at the dayside magnetopause for strongly northward interplanetary magnetic field, *J. Geophys. Res.*, *103*, 6703–6727.

Farrugia, C. J., et al. (2000), Coordinated Wind, Interball/tail, and ground observations of Kelvin-Helmholtz waves at the near-tail, equatorial magnetopause at dusk: January 11, 1997, *J. Geophys. Res.*, *105*, 7639–7667.

Farrugia, C. J., F. T. Gratton, R. B. Torbert, L. Bender, G. Gnavi, K. W. Ogilvie, N. V. Erkaev, R. P. Lepping, and P. Stauning (2003), On the dependence of dayside kelvin-helmholtz activity on IMF orientation, *Adv. Space Res.*, *31*, 1105–1110.

Foullon, C., C. J. Farrugia, A. N. Fazakerley, C. J. Owen, and F. T. Gratton (2010), On the multispacecraft determination of periodic surface wave phase speeds and wavelengths, *J. Geophys. Res.*, *115*, A09203, doi:10.1029/2009JA015189.

Fuselier, S. A., S. M. Petrinec, and K. J. Trattner (2000), Stability of high-latitude reconnection site for steady northward IMF, *Geophys. Res. Lett.*, *27*, 473–476, doi:10.1029/1999GL003706.

Greenstadt, E. W., and J. V. Olson (1976), Pc 3, 4 activity and interplanetary field orientation, *J. Geophys. Res.*, *81*(34), 5911–5920.

Gratton, F. T., L. Bender, C. J. Farrugia, and G. Gnavi (2004), Concerning a problem on the Kelvin-Helmholtz stability of the thin magnetopause, *J. Geophys. Res.*, *109*, A04211, doi:10.1029/2003JA010146.

Hasegawa, A. (1975), *Plasma Instabilities and Non-linear Effects*, Springer, New York.

Hasegawa, H., et al. (2004), Transport of solar wind into Earth's magnetosphere through rolled-up Kelvin-Helmholtz vortices, *Nature*, *430*, 755–758.

Hasegawa, H., et al. (2009), Kelvin-Helmholtz waves at the Earth's magnetopause: Multiscale development and associated reconnection, *J. Geophys. Res.*, *114*, A12207, doi:10.1029/2009JA014042.

Hashimoto, C., and M. Fujimoto (2005), Kelvin-Helmholtz instability in an unstable layer of finite thickness, *Adv. Space Res.*, *37*, 527–531.

Hwang, K.-J., M. M. Kuznetsova, F. Sahraoui, M. L. Goldstein, E. Lee, and G. K. Parks (2011), Kelvin-Helmholtz waves under southward interplanetary magnetic field, *J. Geophys. Res.*, *116*, A08210, doi:10.1029/2011JA016596.

Kivelson, M. G., and S.-H. Chen (1995), The magnetopause: Surface waves and instabilities and their possible dynamical consequences, in *Physics of the Magnetopause*, *Geophys. Monogr. Ser.*, vol. 90, edited by P. Song, B. U. Sonnerup, and M. F. Thomsen, pp. 257–268, AGU, Washington, D. C., doi:10.1029/GM090p0257.

Kuznetsova, M., M. Hesse, D. Sibeck, L. Rastaetter, G. Toth, and T. Gombosi (2008), Non-steady reconnection in global simulations of magnetosphere dynamics, *Eos Trans. AGU*, *89*(53), Fall Meet. Suppl., Abstract SM23C-04.

La Belle-Hamer, A. L., A. Otto, and L. C. Lee (1995), Magnetic reconnection in the presence of sheared flow and density asymmetry: Applications to the Earth's magnetopause, *J. Geophys. Res.*, *100*, 11,875–11,889, doi:10.1029/94JA00969.

Lee, L. C., and J. V. Olson (1980), Kelvin-Helmholtz instability and the variation of geomagnetic pulsation activity, *Geophys. Res. Lett.*, *7*(10), 777–780.

Miura, A. (1995), Dependence of the magnetopause Kelvin-Helmholtz instability on the orientation of the magnetosheath magnetic field, *Geophys. Res. Lett.*, *22*, 2993–2996.

Miura, A., and P. L. Pritchett (1982), Nonlocal stability analysis of the MHD Kelvin-Helmholtz instability in a compressible plasma, *J. Geophys. Res.*, *87*, 7431–7444.

Nakamura, T. K. M., and M. Fujimoto (2008), Magnetic effects on the coalescence of Kelvin-Helmholtz vortices, *Phy. Rev. Lett.*, *101*, 165002.

Nakamura, T. K. M., M. Fujimoto, and A. Otto (2008), Structure of an MHD-scale Kelvin-Helmholtz vortex: Two-dimensional two-fluid simulations including finite electron inertial effects, *J. Geophys. Res.*, *113*, A09204, doi:10.1029/2007JA012803.

Nykyri, K., A. Otto, B. Lavraud, C. Mouikis, L. M. Kistler, A. Balogh, and H. Rème (2006), Cluster observations of reconnection due to the Kelvin-Helmholtz instability at the dawnside magnetospheric flank, *Ann. Geophys.*, *24*, 2619–2643.

Ogino, T. (2009), Plasma instabilities and nonlinear evolution in boundary layers of Earth's magnetosphere, *Eos Trans. AGU*, *90*(52), Fall Meet. Suppl., Abstract SM12A-07.

Omidi, N., D. G. Sibeck, and X. Blanco-Cano (2009), Foreshock compressional boundary, *J. Geophys. Res.*, *114*, A08205, doi:10.1029/2008JA013950.

Otto, A., and D. H. Fairfield (2000), Kelvin-Helmholtz instability at the magnetotail boundary: MHD simulation and comparison with Geotail observations, *J. Geophys. Res.*, *105*, 21,175–21,190, doi:10.1029/1999JA000312.

Paschmann, G., and P. W. Daly (Eds.) (1998), *Analysis Methods for Multi-Spacecraft Data*, *ISSI Sci. Rep. Ser.*, vol. 1, Int. Space Sci. Inst., Bern.

Pickett, J. S., J. R. Franz, J. D. Scudder, J. D. Menietti, D. A. Gurnett, G. B. Hospodarsky, R. M. Braunger, P. M. Kintner, and W. S. Kurth (2001), Plasma waves observed in the cusp turbulent boundary layer: An analysis of high time resolution wave and particle measurements from the polar spacecraft, *J. Geophys. Res.*, *106*, 19,081–19,099, doi:10.1029/2000JA003012.

Russell, C. T., and R. C. Elphic (1978), Initial IEEE magnetometer results: Magnetopause observations, *Space Sci. Rev.*, *22*, 681–715.

Sahraoui, F., et al. (2003), ULF wave identification in the magnetosheath: The k-filtering technique applied to Cluster II data, *J. Geophys. Res.*, *108*(A9), 1335, doi:10.1029/2002JA009587.

Sahraoui, F., G. Belmont, M. L. Goldstein, and L. Rezeau (2010), Limitations of multispacecraft data techniques in measuring wave number spectra of space plasma turbulence, *J. Geophys. Res.*, *115*, A04206, doi:10.1029/2009JA014724.

Sckopke, N., G. Paschmann, G. Haerendel, B. U. Ö. Sonnerup, S. J. Bame, T. G. Forbes, E. W. Hones Jr., and C. T. Russell (1981), Structure of the Low-Latitude Boundary Layer, *J. Geophys. Res.*, *86*(A4), 2099–2110, doi:10.1029/JA086iA04p02099.

Shue, J. H., et al. (1998), Magnetopause location under extreme solar wind conditions, *J. Geophys. Res.*, *103*, 17,691–17,700.

Sibeck, D. G., et al. (1999), Comprehensive study of the magnetospheric response to a hot flow anomaly, *J. Geophys. Res.*, *104*, 4577–4593.

Sibeck, D. G., et al. (2000), Magnetopause motion driven by interplanetary magnetic field variations, *J. Geophys. Res.*, *105*, 25,155–25,169.

Southwood, D. J. (1979), Magnetopause Kelvin-Helmholtz instability, in *Proceedings of the Magnetosphere Boundary Layers Conference*, pp. 357–364, Eur. Space. Agency, Paris.

Thomas, V. A., D. Winske, M. F. Thomsen, and T. G. Onsager (1991), Hybrid simulation of the formation of a hot flow anomaly, *J. Geophys. Res.*, *96*, 11,625–11,632.

Wang, Y. L., R. C. Elphic, B. Lavraud, M. G. G. T. Taylor, J. Birn, C. T. Russell, J. Raeder, H. Kawano, and X. X. Zhan (2006), Dependence of flux transfer events on solar wind conditions from 3 years of Cluster observations, *J. Geophys. Res.*, *111*, A04224, doi:10.1029/2005JA011342.